Geomechanics and Engineering, *Vol. 41, No. 2 (2025) 165-175*
https://doi.org/10.12989/gae.2025.41.2.165

Water infiltration dynamics in bentonite-based engineered barrier systems investigated by time-lapse photography

Jinwoo Kim[1,3], Hwan-Hui Lim*[2], Jin-Seop Kim[1] and Tae-Hyuk Kwon[3]

[1]Disposal Performance Demonstration Research Division, Korea Atomic Energy Research Institute (KAERI), Daejeon 34057, Republic of Korea
[2]Department of Structural Systems & Site Safety Evaluation, Korea Institute of Nuclear Safety(KINS), Daejeon 34045, Republic of Korea
[3]Department of Civil and Environmental Engineering, Korea Advanced Institute of Science and Technology (KAIST), Daejeon 34141, Republic of Korea

(*Received December 6, 2024, Revised March 24, 2025, Accepted March 26, 2025*)

Abstract. The long-term disposal of high-level radioactive waste (HLW) in deep geological repositories requires the reliable performance of engineered barrier systems (EBS). Compacted bentonite, widely used for its high swelling capacity, low permeability, and self-sealing properties, plays a critical role in these barriers. However, understanding the complex coupled thermo-hydro-mechanical (THM) behavior governing water infiltration dynamics remains a significant challenge, especially when gap spaces (or technological voids) are present. This study investigates water infiltration dynamics in bentonite-based EBS using a novel laboratory-scale experimental setup. Time-lapse photography was employed to monitor the evolution of hydration and swelling under thermal gradients and varying gap sizes, simulating repository conditions. The experimental program was designed to compare the effects of two gap sizes on infiltration rates, swelling behavior, and desiccation cracking. Results demonstrated that larger void spaces accommodated greater swelling, leading to lower dry density and higher permeability, while smaller gaps restricted desiccation cracking due to mechanical constraints. The correlation between pixel intensity and water content allowed the derivation of a linear calibration model, enabling real-time, non-destructive estimation of moisture distribution in bentonite. Findings in this study highlight the interplay between gap size, water infiltration, and thermal effects, emphasizing the need for optimized EBS designs to balance mechanical integrity and hydraulic performance. It is anticipated that the insights provided by this study contribute to the refinement of predictive models and advancing the safe and effective containment of HLW over geological timescales.

Keywords: bentonite; engineered barrier systems; gap space; high-level radioactive waste disposal; THM behavior; water infiltration

1. Introduction

The long-term disposal of high-level radioactive waste (HLW) in deep geological repositories is a key concern for nuclear waste management programs worldwide (Sellin and Leupin 2013, Posiva 2021, SKB 2022, Lee *et al.* 2007, Kim *et al.* 2021). Ensuring the containment and isolation of these hazardous materials over hundreds of thousands of years is a formidable challenge, particularly in the design of engineered barrier systems (EBS). The EBS, which typically comprises compacted bentonite clay, plays a crucial role in minimizing the migration of radionuclides into the surrounding geological environment. Bentonite is favored for its inherent properties such as high swelling potential, low permeability, and the capacity to self-seal, making it an effective barrier against water infiltration and radionuclide transport (Börgesson *et al.* 2001, Pusch 2006, Yoon *et al.* 2021, Yoon *et al.* 2023).

Water infiltration into the EBS involves complex coupled thermo-hydro-mechanical (THM) interactions. Fig. 1 provides schematic illustrations of these interactions within the concept of the improved Korean Reference Disposal System (KRS$^+$; Lee *et al.* 2007, Lee *et al.* 2020). Upon contact with groundwater from the adjacent host rock, compacted bentonite undergoes hydration and swells, filling voids and microfractures, thereby enhancing its sealing properties (Sellin and Leupin 201`3). This swelling behavior is essential for maintaining containment integrity, especially in the presence of gap spaces (or technological voids) or desiccation cracks developing from thermal stresses from the decay heat generated by HLW canisters (Börgesson *et al.* 2017). However, the dynamic nature of this process—particularly under the coupled THM interactions—presents significant challenges for predicting long-term barrier performance.

The complexities of the THM processes in bentonite arise from the strong interdependence of temperature, degree of saturation, mechanical stress, and the microstructure (Shawn 2023). Elevated temperatures from the decaying radioactive material alter the water retention capacity and hydraulic conductivity of bentonite, while also affecting the rates of swelling and shrinkage (Jain 2024, Kim *et al.* 2021, Yoon *et al.* 2022). Water infiltration initiates a sequence of physicochemical interactions within the bentonite matrix, including osmotic swelling, hydration of clay minerals, and the redistribution of pore water

---

*Corresponding author, Senior researcher
E-mail: hwanhui@alumni.kaist.ac.kr

http://www.techno-press.org/?journal=gae&subpage=7

ISSN: 2005-307X (Print), 2092-6219 (Online)

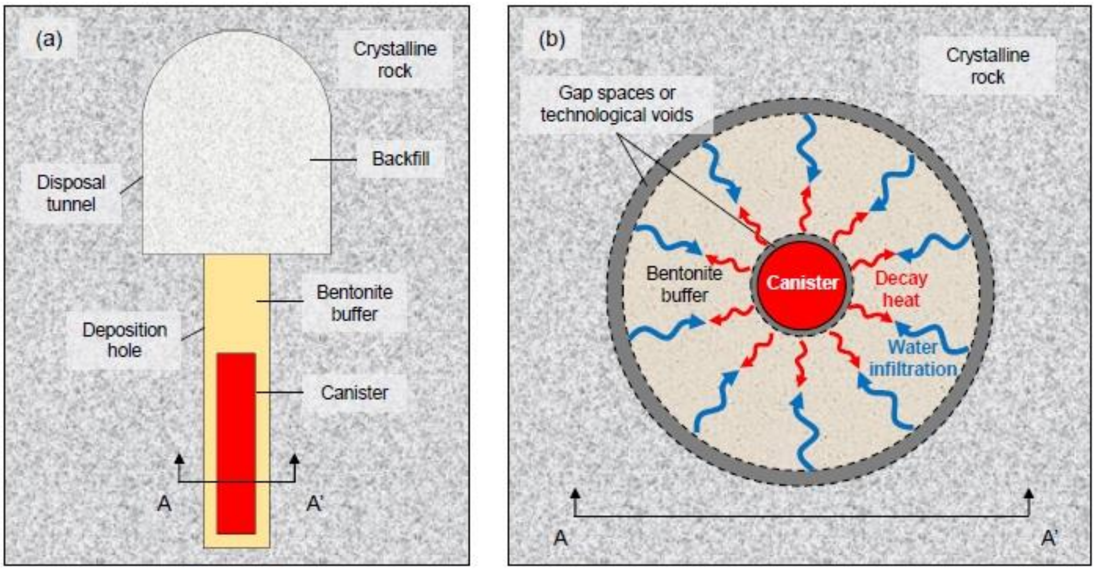

Fig. 1 Schematic illustrations of (a) the improved Korean reference disposal system (KRS$^+$) for high-level radioactive wastes and (b) ground water infiltration into the engineered barrier system under thermal gradients

(Dueck and Börgesson, 2015). These coupled interactions are further influenced by site-specific geological conditions, such as the proximity to groundwater, rock permeability, and the nature of host rocks, which can introduce variability in infiltration behavior (Kim *et al.* 2019).

To address these complexities, experimental studies are indispensable in understanding the coupled THM behavior of bentonite and refining the predictive models to ensure the intended performance of the EBS over geological time scales (Gens *et al.* 2009). While in-situ tests in a simulated nuclear waste repository provide valuable experimental evidences about the evolution of THM properties of bentonite, it can be very time-consuming (Villar *et al.* 2018, Villar *et al.* 2020, Kim *et al.* 2023b). Alternatively, laboratory tests performed in controlled environments can offer insights into the hydration kinetics, swelling dynamics, and the evolution of mechanical properties of bentonite under different temperatures and saturation regimes (Diaz *et al.* 2023, Kim *et al.* 2023a). However, replicating in-situ conditions and accurately modeling the long-term evolution of the THM properties of bentonite face significant challenges (Min and Yoon 2024).

In recent years, digital imaging has emerged as an effective technique for estimating soil water content, complementing traditional methods (e.g., oven drying) that are often destructive and lack spatial detail. As a non-destructive, high-resolution technique, digital imaging has been successfully used to predict the surface water content from the soil color (Persson 2005, Baek *et al.* 2024) and the hyperspectral imaging (Lim *et al.* 2020). For bentonite, time-lapse photography has been used to monitor and analyze the morphological changes in bentonite during hydration (Wang *et al.* 2021, Meng *et al.* 2023).

In this study, the water infiltration dynamics in a bentonite-based EBS is investigated under controlled THM conditions. A novel experimental approach combining water infiltration tests with time-lapse photography has been developed to monitor the water content changes in bentonite. In particular, the infiltration tests were designed to highlight the role of gap spaces by controlling the gap sizes. The reason for controlling the gap size is that it significantly influences water infiltration rates, swelling behavior, and crack development, all of which are critical factors affecting the long-term performance of engineered EBS in HLW disposal (Li *et al.* 2023). In the following, the material used as well as the experimental setup and the image analysis procedure are described. The obtained results are presented and discussed, focusing on the effect of gap sizes.

2. Material and methodology

2.1 Specimen preparation

In this study, Bentonil-WRK, a commercial calcium-type bentonite, has been used to prepare test specimens used for the experiments. Recently, Bentonil-WRK has been widely studied as a candidate buffer material (Lee *et al.* 2023, Lee *et al.* 2024, Yoon *et al.* 2024). Among others, Yoon et al. (2024) reported its material properties from through characterization. In terms of mineralogical composition, Bentonil-WRK contains 69–73 wt.% montmorillonite as its primary component, along with 14 wt.% albite, 2 wt.% quartz, and 13 wt.% cristobalite as secondary minerals. Some geotechnical properties are listed in Table 1. The hygroscopic water content of Bentonil-WRK measured by oven-drying was 13.45%, and the specific gravity was 2.55. To prepare test specimens, bentonite powder has been compacted by the cold isostatic press (CIP) method, which has shown good performances in fabricating homogeneous bentonite blocks (Kim *et al.* 2018). Two test specimens were prepared in a thin hollow disc shape. The dimensions of the test specimens will be described in details in 2.3. The

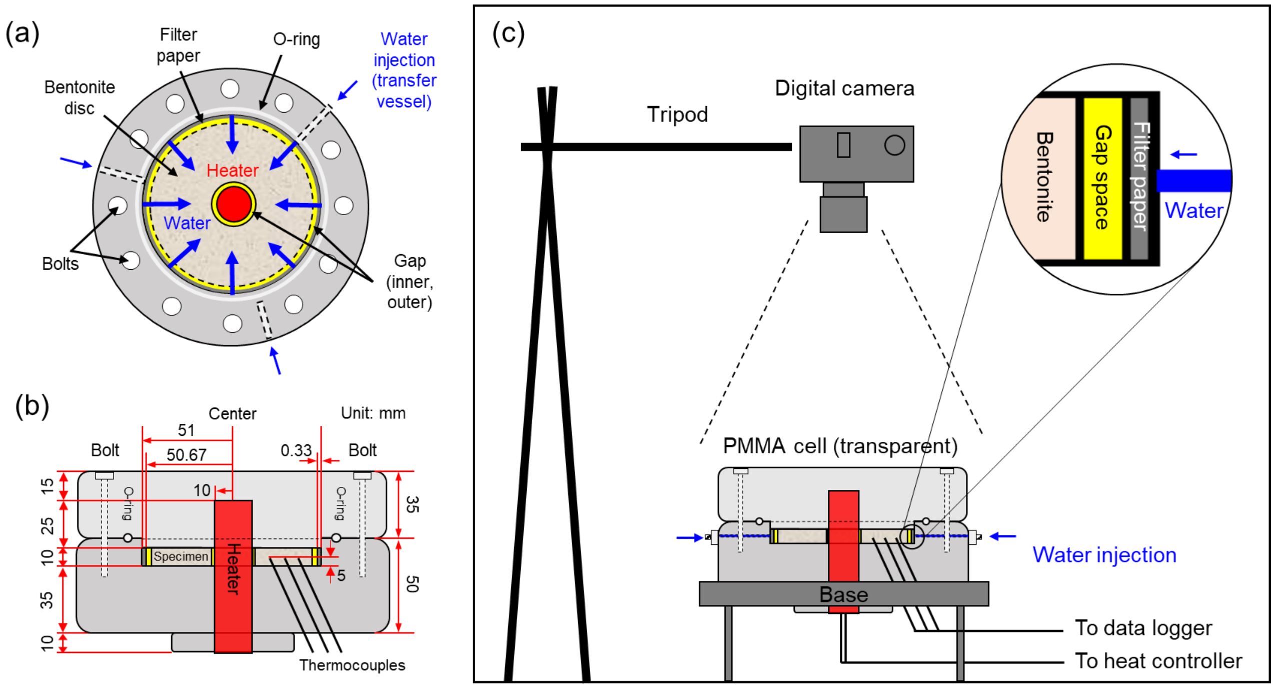

Fig. 2 Schematic illustrations of the experimental setup: (a) top view of the cell, (b) cross-sectional view of the cell and (c) overview showing the cell with a heater, water injection lines, a camera, and thermocouples

Table 1 Geotechnical properties of Bentonil-WRK

Properties	Units	Values
Water content (hygroscopic)	[%]	13.45
Specific gravity	[-]	2.55
Plastic limit	[%]	42.4
Plastic index	[%]	54.7
United Soil Classification System (USCS)	[-]	MH

target water content and dry density were 14% and 1.7 g/cm^3, respectively (see Table 2).

2.2 Experimental setup

An experimental setup was designed to visually capture and analyze the intricate water infiltration dynamics in EBS, under controlled THM conditions representative of those in deep geological repositories. Fig. 2 provides schematic illustrations of the developed experimental setup, including a test cell and a digital camera. In particular, the setup was designed to control thermal gradients by a central heater, water injection pressure and rate, bentonite dry density, and gap widths, simulating the environmental conditions in EBS. The novelty of the developed experimental setup is the use of time-lapse photography that allows for non-destructive monitoring of water content in real-time.

The test cell (Figs. 2(a) and 2(b)) was equipped with a heating and a water injection system. The cell had a cylindrical empty space that was 102 mm in diameter and 10 mm thick, and the central heater was 20 mm in diameter.

Table 2 List of tests performed and their initial conditions

			Small Gap Test	Large Gap Test
Specimen size	**Outer diameter**	[mm]	98	94
	Inner diameter	[mm]	22	26
	Thickness	[mm]	10	10
Gap size	**Outer gap**	[mm]	1.7	3.7
	Inner gap	[mm]	1	3
	Thickness	[mm]	10	10
Specimen dry density (initial conditions)		**[g/cm^3]**	1.70	1.70
Water content		**[%]**	14	14
Heater temperature		**[°C]**	85	85

A heat controller was used to adjust the power supplied to the heater. This allowed for the simulation of thermal loads representative of radioactive decay heat in deep geological repositories. Since the test specimens were smaller than the inner space of the cell, mounting a specimen resulted in gaps. These gaps—between the cell and the specimen and between the heater and the specimen—were intentionally left empty to represent gap spaces in engineered barrier systems. Two layers of filter papers (0.33 mm thick) were placed around the specimen to ensure uniform distribution of injected water and to avoid the potential loss of bentonite. Along the perimeter of the cell, three water injection ports were distributed symmetrically. The injection ports allowed controlled water infiltration into the cell, simulating different hydration scenarios. The cell was closed by multiple stainless-steel bolts and tightly sealed with a rubber O-ring to prevent water leakage. This prevented the bentonite from vertically swelling upon hydration, whereas horizontal swelling was accommodated by both outer and inner gaps that were intentionally created to represent the gap space in engineered barrier systems. The test cell was made of transparent polymethyl methacrylate (PMMA), which provided excellent visibility for monitoring the water infiltration dynamics inside the cell.

An overview of the entire experimental setup is shown in Fig. 2(c). Temperatures were locally measured by thermocouples. One thermocouple was installed inside the heater and was connected to the heater for servo-control (TC0). A set of three thermocouples (TC1, TC2, and TC3) were embedded into the specimen at different distances from the heater (20 mm, 30 mm, and 40 mm, respectively) by drilling holes and filling them by thermal paste. The temperatures were recorded every 10 min by a digital logger. The ambient temperature in the lab was controlled to 25°C. For water injection, deionized water was injected under a back pressure of 100 kPa using a transfer vessel and distributed to each injection port. The applied back pressure of 100 kPa enabled the tests to be conducted within an affordable timeframe of a few weeks.

The test cell was placed directly under a digital camera (100D, Canon, Tokyo, Japan) mounted on a tripod. Digital images were obtained using the camera set to a f-stop of f/3.5, an exposure time of 1/8 second, an ISO speed of ISO-100, ensuring high-resolution images under controlled lighting conditions. The setup was placed inside a darkroom to prevent reflections of the lights on the top surface of the cell, while one side was open for lighting. A reflector was installed on the opposite side of the light source to ensure that indirect lighting reached the entire setup. The obtained images were RGB and 5184*3436 pixel with a resolution of 1.2 mm/pixel. The imaging intervals were 1 h. The time-lapse digital images were used for subsequent analysis of the temporal evolution of hydration and drying patterns.

2.3 Water infiltration tests

Water infiltration tests were conducted to observe the infiltration dynamics in bentonite-based engineered barrier systems under controlled THM conditions. In particular, two tests with different gap sizes were conducted to investigate the role of gap spaces, as shown in Table 2. Given the sizes of a deposition hole (1,750 mm) and a disposal canister (1,030 mm) in the KRS$^+$ concept (Lee *et al.* 2020), the infiltration distance close to 40 mm is approximately a 9:1 downscaled representation of the EBS design in KRS$^+$. Thus, the outer gaps of 1.7 mm and 3.7 mm would correspond to 14.8 mm and 32.5 mm gaps between the bentonite block and the crystalline rock, respectively. Similarly, the inner gaps of 1 mm and 3 mm would represent 8.9 mm and 26.6 mm gaps between the bentonite blocks and the canister.

2.3.1 Heating phase

A bentonite specimen was assembled inside the cell. After assembling, the cell was closed to vertically confine the bentonite disc, and vacuum was applied to evacuate air from the system by a vacuum pump to avoid water blocking. The water valves were closed after at least 30 min of vacuuming. The heater temperature was increased step-wise, increasing the heater temperature from the ambient temperature of 25°C to 45°C, 65°C, and 85°C. The final heater temperature of 85°C reflects the estimated temperature inside the EBS in the KRS$^+$ system (Kim *et al.* 2021). Each step was continued until the temperatures measured indicated attainment of thermal equilibrium. Although measured temperatures became stable within only few hours at all steps, extra time was given to reach complete thermal equilibrium. Consequently, each step was maintained for at least 10 hours (Small Gap test) or 4 hours (Large Gap test).

2.3.2 Injection phase

The injection phase started by injecting water under a constant pressure of 100 kPa by opening the water valve. Deionized water was instantaneously pulled into the cell by the vacuum and the back pressure. As water infiltrated the bentonite, the color of the bentonite was expected to become darker with increasing water content (Persson 2005, Baek *et al.* 2024). This injection phase continued for 20 days, which was sufficient to observe no further color change.

2.3.3 Sampling phase

Finally, the heater was turned off, the cell was opened, and the bentonite specimen was sampled at various locations. Sampling was performed carefully by inserting stainless-steel samplers into the specimen to obtain undisturbed samples. Samples were oven-dried for at least 72 h to determine gravimetric water contents. The initial and final water contents provided reference values for calibration of the water content estimated from the image analysis.

2.4 Image analysis

2.4.1 Image acquisition and post-processing

The time-resolved digital images were downscaled by a factor of 0.25, translated to align the center of the heater with the center of the frame, cropped to the central region of 800*800 pixels, and saved as a TIFF stack using the open-source software ImageJ (Schneider *et al.* 2012). The TIFF stack therefore had a dimension of 800*800*t, where t is the number of images equal to the time of the test in hours. The TIFF stack was imported and processed by a custom-made MATLAB script. Exposure corrections were performed for fluctuations in image brightness across different frames. The correction was applied by calculating the average pixel value within a reference region outside the cell where no change in color is expected and by adjusting the entire image based on the deviation from a specified reference value.

2.4.2 Calculation of average pixel value (APV)

From the TIFF image stack, average pixel values (APV) were calculated and used to estimate the water content of the specimen. A grid representing the pixel coordinates of

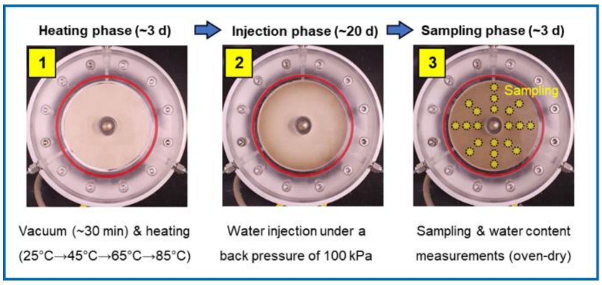

Fig. 3 Adopted procedure for water infiltration tests

the image was generated to determine the distance of each pixel from the center of the image. This distance was calculated as the square root of the sum of the squared differences in x and y coordinates, and subsequently converted to physical units (mm) using a factor which was 334 pixels per 100 mm in this case. For each image in the stack, the APV at a given distance from the center r was computed by averaging the pixel value (PV) over orientations θ of 0-360°. The APV therefore represented the extent of water infiltration and its distribution in the specimen.

2.4.3 Estimation of water content

The water content w of the specimen was estimated from the APV. The w-APV relationship was calibrated using the reference water content values measured at the beginning and the end of the tests and the sum of pixel values over the regions of samples. This calibration was performed while assuming a linear relationship between the water content and the APV (e.g., Attarzadeh *et al.* 2018, Burgis *et al.* 2018, Bertalan *et al.* 2022). This enabled conversion of APV profiles to corresponding water content profiles throughout the infiltration period.

3. Results and analysis

3.1 Heating phase results

Fig. 4 illustrates the temporal and spatial evolution of the local temperatures during the heating phase. In both tests, temperature readings from the thermocouples TC1, TC2, and TC3 embedded at 20, 30, and 40 mm from the heater, respectively, indicated that the local temperatures were reaching steady-state conditions within approximately 100 min after each step. Higher temperature near the heater was evident, with the Small Gap test showing a comparable temperature gradient compared to the Large Gap test. The temperature difference measured between TC1 (20 mm from the heater) and TC3 (40 mm from the heater) was 14.8°C in the Small Gap test whereas the difference was 14.5°C in the Large Gap test. This indicated that the larger gap size did not necessarily reduce the heat conduction to the bentonite buffer.

Fig. 5 shows the visual observations made during the heating phase for both tests. The Small Gap test did not exhibit any visible cracks throughout the heating phase, even when the heater temperature increased to 85°C. In

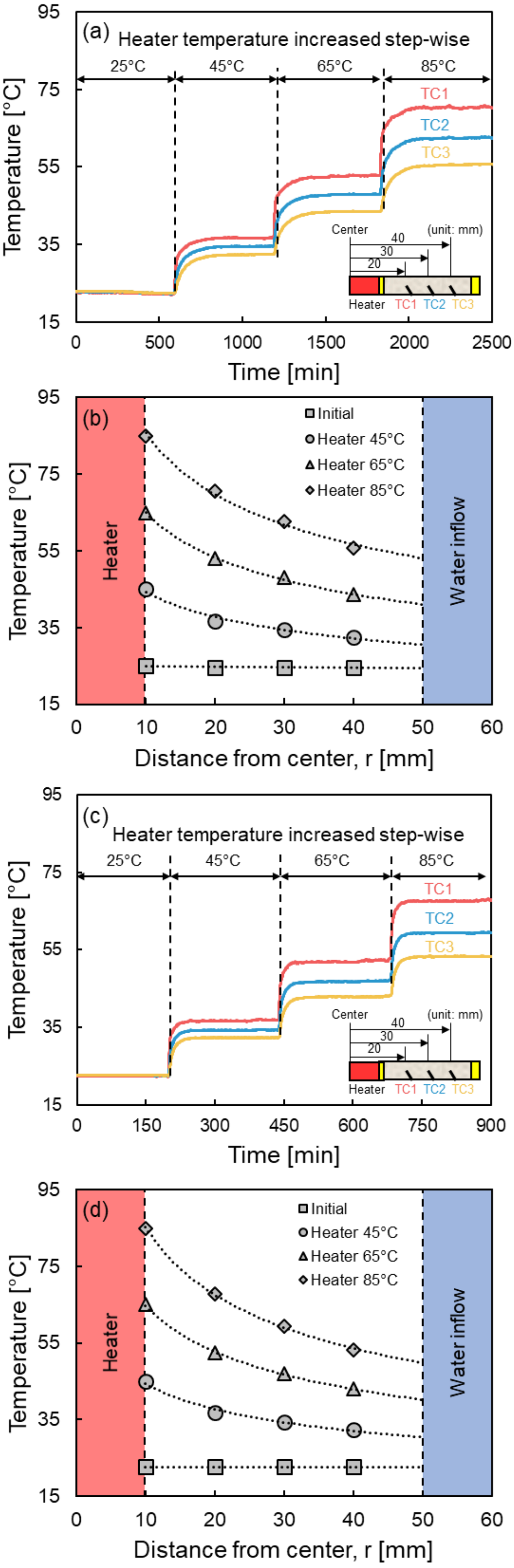

Fig. 4 Time-series temperature data and temperature profiles during the heating phase of (a) the Small Gap test and (b) the Large Gap test

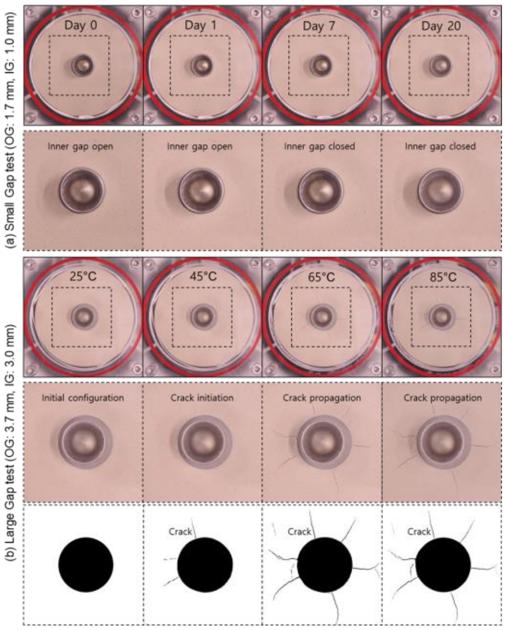

Fig. 5 Time-lapse photographs and during the heating phase at heater temperatures of 25, 45, 65, and 85°C and thresholded black and white images highlighting the crack morphology (bottom row)

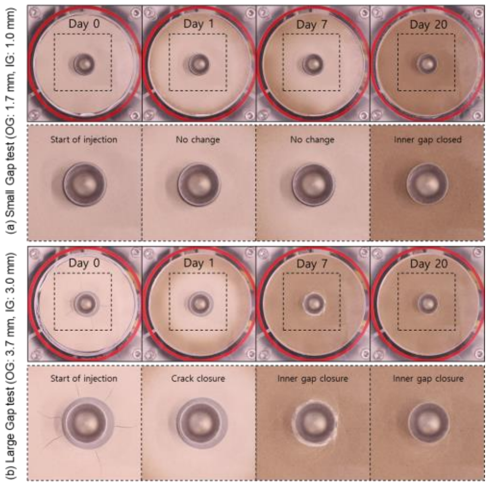

Fig. 6 Time-lapse photographs during the injection phase at Day 0, 1, 7, and 20

contrast, the Large Gap test showed pronounced desiccation cracking. At an initial temperature of 25°C, the bentonite specimen appeared intact. As the temperature was increased to 45°C, thin cracks appeared near the heater in a radial pattern. When the heater temperature was increased to 65°C, these cracks grew and propagated outward, and additional cracks were formed. Six main crack networks were relatively evenly distributed, approximately 60 degrees apart from each other. The crack configuration was largely unchanged at a higher heater temperature of 85°C, suggesting that a critical heater temperature for the observed desiccation cracks in the given configuration was between 45°C and 65°C.

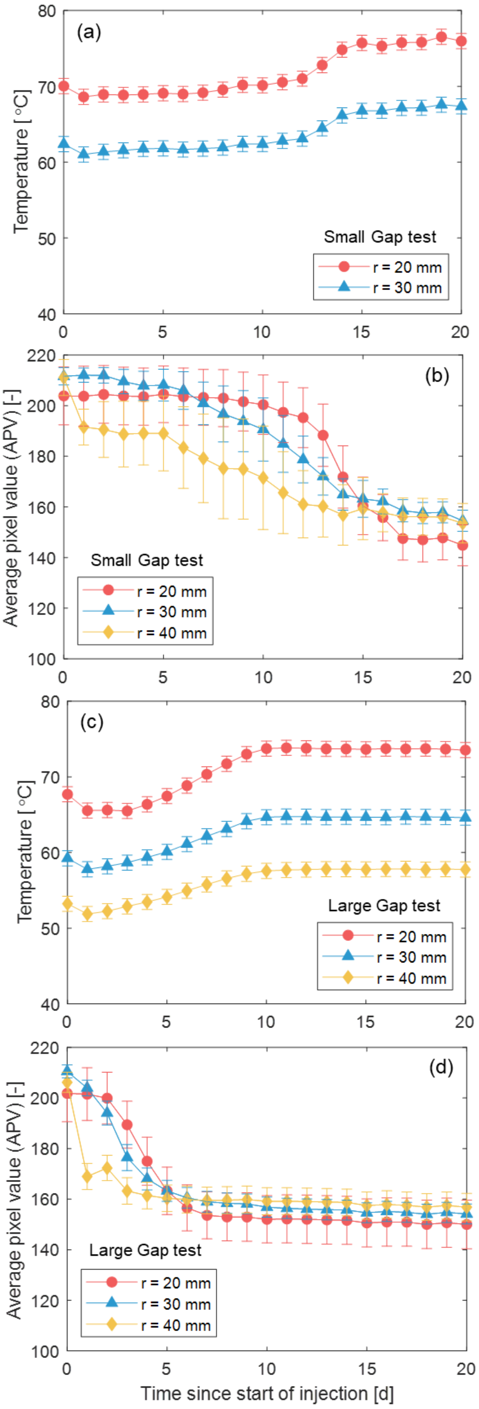

Fig. 7 Temporal evolutions of temperatures and the calculated average pixel value (APV) during the injection phase of (a)-(b) the Small Gap test and (c)-(d) the Large Gap test

3.2 Injection phase results

The injection phase results of both Small Gap and Large Gap tests in Fig. 6 highlight the coupled hydro-mechanical behavior of a bentonite-based EBS to water infiltration under varying gap sizes. In both tests, as soon as valves were opened, water was pulled into the cell and filled the outer gap. As water infiltrated into the bentonite, the outer

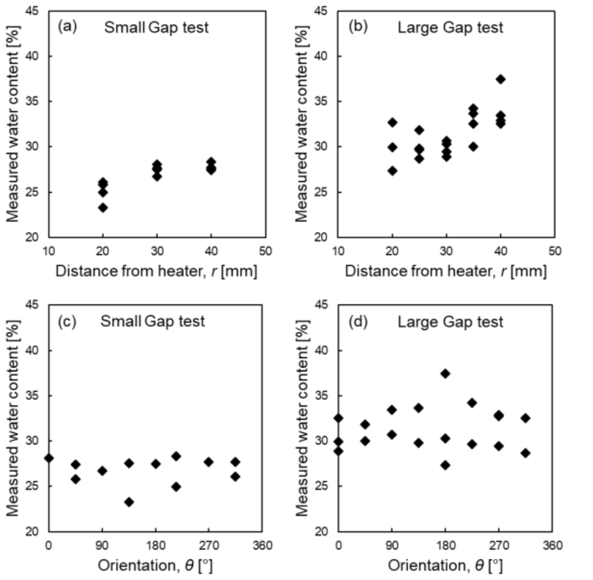

Fig. 8 Final measured water contents at different distances from the heater and orientations

gaps between the bentonite and the cell were quickly filled by swelling. More interesting observations could be made regarding the inner gaps between the bentonite and the heater. During the Small Gap test, no significant changes were observed in the early stages after water injection began (Day 1 and Day 7), indicating water infiltration was limited to the outer region of the bentonite. By Day 7, the water front was found advanced, yet the inner gap was still present. By Day 20, the bentonite disc appeared darker, and the inner gap was completely filled. In contrast, the Large Gap test started on with cracks from the heating phase on Day 0. On Day 1, the water front appeared to be advancing more quickly, indicating a markedly higher infiltration rate due to the lower average dry density of the bentonite. The desiccation cracks near the heater were closed, likely due to the swelling pressure developed in the outer region. By Day 7, the water front appeared to have reached the inner gap, which was starting to be filled by swelling. By Day 20, the inner gap was completely closed.

The time-series plots in Fig. 7 illustrate the evolution of temperature and APV with time during the injection phase. Error bars in the temperature data represent the measurement accuracy of the thermocouples, while error bars in the APV data represent the standard deviation of pixel values at given distances from heater. In the Small Gap test, unfortunately, the thermocouple TC3 at r = 40 mm was not responsive and the temperature data was not available. Nevertheless, the temperatures at r = 20 mm and 30 mm indicated clear thermal gradient throughout the injection phase, with higher temperatures recorded at positions closer to the heater. The temperatures were stable and gradually increased during 12-15 days since the start of injection. The higher temperatures were expected as an outcome of the thermal conductivity increasing with water content (Yoon *et al*. 2024). This coincided with the water infiltration into the bentonite observed by the decreases in APV. The APV values decreased as the bentonite became darker due to water infiltration. The early reduction in APV at r = 40 mm shows water reaching the outer region and followed by the onsets of reduction at r = 30 and 40 mm. In the Large Gap test, temperatures showed, again, clear thermal gradients. The temperatures increased during 5-10 days since the start of injection. However, the APV started to decrease earlier during 0-5 days since the start of injection. The delayed increases in temperatures indicates the time required to reach thermal equilibrium after the rapid changes in water content and degree of saturation. The error bars in the APV data indicate the magnitude of noise caused by the pixel-scale variation of greyvalue (i.e., texture) and noise in the captured digital image. Moreover, the larger error bars during the Small Gap Test suggest that there was some localized water infiltration leading to additional variation with orientation. Nevertheless, the APV captured well the general trends of water infiltration dynamics.

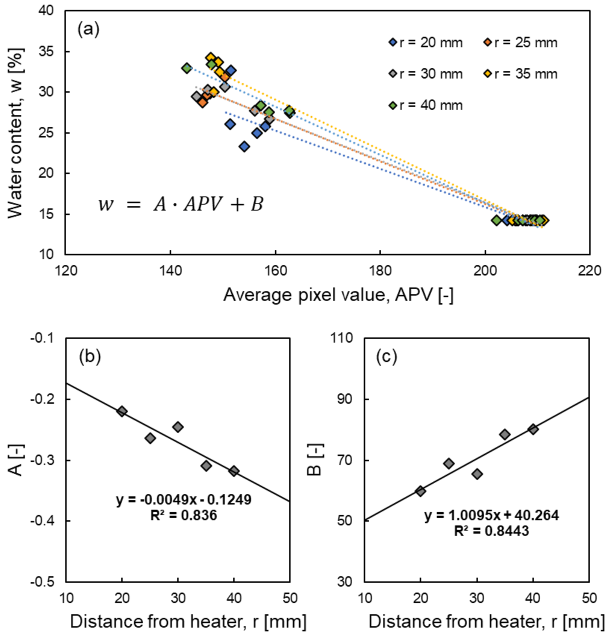

Fig. 9 (a) Calibration equations obtained by linear regressions for the water content-average pixel value relationships for different distances from the heater and (b)-(c) calibration parameters A and B dependencies on distances from the heater

3.3 Sampling and calibration

Fig. 9 presents the water content measurements from bentonite samples collected at various locations after the injection phase, plotted against the distance from the heater, *r*, and the orientations, *θ*. In the Small Gap test, the measured water contents increased slightly with *r*, ranging from 23% to 28%. For the large gap test (Fig. 9), the measured water contents showed slightly larger variation with *r*, ranging from 27% to 37%. The common trend of generally higher water contents at farther distances from the heater is likely a result of heat-induced moisture migration. The overall higher water contents in the Large Gap tests

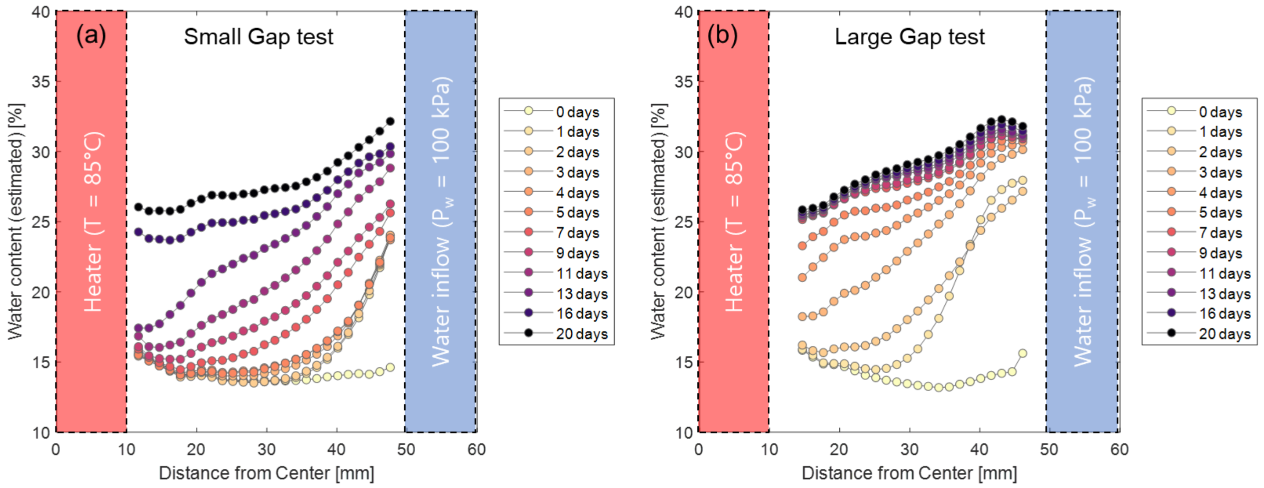

Fig. 10 Temporal evolutions of the estimated water content profiles during the infiltration phase of (a) the Small Gap test and (b) the Large Gap test

indicates larger average void ratios after swelling. On the other hand, for both tests, the measured water contents appeared relatively consistent across different orientation angles, confirming that the water infiltration was relatively homogenous and had no preferential orientation. The differences in water content at the same orientation represent the variation of water content with distance from the heater. It is also likely that these differences were caused by slight disturbances during the sampling process in adjacent locations.

The relationship between measured water content, w, and APV was calibrated for different distances from the heater, as shown in Fig. 8. Linear regression was used to derive the calibration equations of the following form for different positions:

$$w_{est} = A*APV + B$$

where w_{est} is the estimated water content, A and B are the calibration parameters, and APV is the average pixel value. The calibrated parameters showed differences with respect to the distance from the heater, indicating that the w-APV relationship was influenced by the differences in lighting conditions, temperature, and dry density, among others. These dependencies on distance from the heater showed systematic variation in the calibration parameters A and B, which can be also defined by linear regression as shown in Fig. 9. However, it should be acknowledged here that the calibration equations were derived from only one initial water content. More data with water content values in between the initial and the final conditions are warranted to have more detailed calibration equations for more accurate estimation of the water content.

4. Discussion

4.1 Evolution of water content profiles

Fig. 10 shows the evolution of estimated water content profiles across the bentonite specimen during the injection phase for both tests. The water content profiles are presented for select times between 0 and 20 days since the start of water injection. In both tests, the water contents increase quickly near the water inflow, indicating early water infiltration into outer region of the bentonite. The evolutions of the water content profiles illustrate well the advancing water front toward the center. Distinct differences in the infiltration patterns were observed between the two tests. In the Small Gap test (Fig. 10(a)), the water front reached the inner gap between Day 11 and Day 13. In contrast, the Large Gap test (Fig. 10(b)) exhibited more rapid infiltration, with the water front reaching the inner gap between Day 2 and Day 3. The markedly higher infiltration rate in the Large Gap test can be attributed to the larger initial void space accommodating greater swelling, leading to lower average dry density and therefore higher permeability (Cho *et al.* 1999, Park *et al.* 2021).

Comparing the final estimated water content profiles on Day 20 in Fig. 10 with the measured water content profiles in Fig. 8, the estimated profiles show broad agreement with the measured ones. However, the initial estimated profiles on Day 0 seem to fail in capturing the water content near the heater for both tests by suggesting higher water contents near the heater, which is unlikely considering the lower water contents near the heater reported from in-situ tests (Villar *et al.* 2018, Villar *et al.* 2020, Kim *et al.* 2023). This suggests limitations in the calibration equations assuming linear dependencies exclusively on APV, neglecting the potential influences of temperature and dry density.

4.2 Gap-controlled water infiltration in EBS

The contrasting results of the two water infiltration tests in this study highlight the critical role of gap spaces (technological voids) during water infiltration into bentonite-based EBS. Initially, an EBS may consists of a bentonite buffer of a dry density of 1.7 g/cm^3 and annular gap spaces, both inner and outer. After the emplacement, the inner region of the bentonite buffer may experience desiccation cracking due to the heat, while the outer gap will accommodate groundwater inflow. The size of inner gap is likely to control the extent of desiccation cracking (Fig. 5). However, the visual observation during the heating phase of the Large Gap test in this study (Fig. 5) suggests that the desiccation cracks are likely to be closed quickly by the swelling pressure generated from the outside of the buffer before water reaches the cracks. A critical inner gap size for balancing the mechanical boundary conditions with the tensile stresses driving desiccation cracks (Peron *et al.* 2009, Peron *et al.* 2009) should be therefore understood in conjunction with the rate of water infiltration and swelling pressure development. Notably, these are largely influenced by the size of outer gap enhancing the local hydraulic conductivity through swelling as well as potential post-piping cracking (Lee *et al.* 2024). This sequence underlines the importance of optimizing gap sizes or using appropriate gap-filling materials in repository designs to ensure effective sealing, also because from a construction feasibility standpoint larger gaps facilitate the emplacement of the bentonite buffer.

5. Conclusions

This study investigated the water infiltration dynamics in bentonite-based engineered barrier systems (EBS) for deep disposal of high-level radioactive waste (HLW). Understanding the gap-controlled water infiltration dynamics under controlled thermo-hydro-mechanical (THM) conditions is essential for optimizing the design and performance of EBS in deep geological repositories.

The main contributions of this study can be summarized as follows:

- An experimental setup was developed to visually monitor water infiltration dynamics in EBS using time-lapse photography for non-destructive, real-time observation of cracking, swelling, and water content changes.
- Downscaled (9:1) experiments allowed the water infiltration to be reproduced within an affordable time scale of a few weeks. This offered a great advantage for bridging the gap between laboratory-scale and engineering- or field-scale testing, which typically require significantly longer durations up to years.
- The contrasting results obtained for different gap sizes suggest that the larger gap spaces (technological voids) affect the infiltration process by 1) increasing the likelihood of thermal cracks near the heater, 2) enhancing the rate of early water infiltration from the host rock, and 3) enhancing heat conduction.
- By analyzing the correlation between average pixel value and water content, an empirical relationship was developed to estimate the water distribution in bentonite over the course of infiltration processes. Such an approach offers significant advantages in terms of spatial resolution and real-time monitoring.

The main findings in this study regarding the role of gap spaces (technological voids) highlight the importance of optimizing gap sizes in EBS design to balance mechanical integrity and hydraulic performance. Even if compacted bentonite blocks are manufactured homogeneously and emplaced in intact conditions, the presence of gap spaces (technological voids) is likely to introduce localized behavior that cannot be readily captured by current numerical simulation schemes at the continuum scale.

The ongoing research by the authors aims to extend the experimental investigation to include the effect of gap-filling materials and to develop advanced numerical models capable of reproducing the localized effects. Future work will focus on modeling the gap-controlled THM behavior, with the goal of bridging the gap between laboratory observations and field-scale predictions by taking into account the scale effects.

Acknowledgments

This work was supported by the National Research Foundation of Korea (NRF) grant funded by the Korea government (MSIT)(RS-2024-00340851). J. Kim (partially) and J.-S. Kim were supported by the Nuclear Research and Development Program of the National Research Foundation of Korea (2021M2E1A1085193).

References

Attarzadeh, R., Amini, J., Notarnicola, C. and Greifeneder, F. (2018), “Synergetic use of Sentinel-1 and Sentinel-2 data for soil moisture mapping at plot scale”, *Remote Sens.*, **10**(8), 1285. https://doi.org/10.3390/rs10081285

Baek, S.H., Jeon, J.S. and Kwak, T.Y. (2024), “Prediction of soil composition using digital images taken under variable lighting environments”, *KSCE J. Civil Eng.*, **29**(4), 100093.

Bertalan, L., Holb, I., Pataki, A., Négyesi, G., Szabó, G., Szalóki, A.K. and Szabó, S. (2022), “UAV-based multispectral and thermal cameras to predict soil water content–A machine learning approach”, *Comput. Electron. Agricult.*, **200**, 107262. https://doi.org/10.1016/j.compag.2022.107262.

Börgesson, L., Chijimatsu, M., Fujita, T., Nguyen, T.S., Rutqvist, J. and Jing, L. (2001), “Thermo-hydro-mechanical characterisation of a bentonite-based buffer material by laboratory tests and numerical back analyses”, *Int. J. Rock Mech. Min. Sci.*, **38**(1), 95-104. https://doi.org/10.1016/S1365-1609(00)00067-8.

Börjesson, P., Hansson, J. and Berndes, G. (2017), “Future demand for forest-based biomass for energy purposes in Sweden”, *Forest Ecol. Management*, **383**, 17-26. https://doi.org/10.1016/j.foreco.2016.09.018.

Burgin, M.S., Mandrake, L., Doran, G.B., Bue, B.D. and Van Zyl, J.J. (2018), “Soil moisture estimation by linear regression from smap polarimetric radar data with aquarius derived coefficients”, *Proceedings of the IGARSS 2018-2018 IEEE International Geoscience and Remote Sensing Symposium*, IEEE. https://doi.org/10.1109/IGARSS.2018.8518488.

Cho, W.J., Lee, J.O. and Chun, K.S. (1999), "The temperature effects on hydraulic conductivity of compacted bentonite", *Appl. Clay Sci.*, **14**(1-3), 47-58. https://doi.org/10.1016/S0169-1317(98)00047-7.

Diaz, M.B., Kim, S.S., Lee, G.W., Kim, K.Y., Lee, C., Kim, J.S. and Kim, M. (2023), "Physio-mechanical and X-ray CT characterization of bentonite as sealing material in geological radioactive waste disposal", *Geomech. Eng.*, **34**(4), 449-459. https://doi.org/10.12989/gae.2023.34.4.449.

Gens, A., Sánchez, M., Guimarães, L.D.N., Alonso, E.E., Lloret, A., Olivella, S. and Huertas, F. (2009), "A full-scale in situ heating test for high-level nuclear waste disposal: observations, analysis and interpretation", *Géotechnique*, **59**(4), 377-399. https://doi.org/10.1680/geot.2009.59.4.377.

Jain, A.K. (2024), "Exploring the viability of Bentonite-amended blends incorporating marble dust, sand, and fly ash for the creation of an environmentally sustainable landfill liner system", *Int. J. Geo-Eng.*, **15**(1), 16. https://doi.org/10.1186/s40703-024-00214-4

Kim, M.S., Jeon, J.S., Kim, M.J., Lee, J. and Lee, S.R. (2019), "A multi-objective optimization of initial conditions in a radioactive waste repository by numerical thermo-hydro-mechanical modeling", *Comput. Geotech.*, **114**, 103106. https://doi.org/10.1016/j.compgeo.2019.103106.

Kim, M., Lee, S., Cheon, E., Kim, M. and Yoon, S. (2021), "Thermochemical changes on swelling pressure of compacted bentonite", *Annal. Nucl. Energ.*, **151**, 107882. https://doi.org/10.1016/j.anucene.2020.107882.

Kim, M., Lee, S., Kim, J. and Yoon, S. (2023a), "Effects of initial compaction condition and temperature on swelling characteristics of compacted bentonite", *Prog. Nucl. Energ.*, **164**, 104871. https://doi.org/10.1016/j.pnucene.2023.104871.

Kim, M., Kim, G.Y., Kim, J.S., Yoon, S., Lee, C., Lee, D. and Hong, E.S. (2023b), "Evaluation of changes in buffer properties from an in-situ engineered barrier experiment", *Appl. Clay Sci.*, **244**, 107092. https://doi.org/10.1016/j.clay.2023.107092.

Kim, K.I., Lee, C. and Kim, J.S. (2021), "A numerical study of the performance assessment of coupled thermo-hydro-mechanical (THM) processes in improved Korean reference disposal system (KRS+) for high-level radioactive waste", *Tunn. Undergr. Sp.*, **31**(4), 221-242. https://doi.org/10.7474/TUS.2021.31.4.221.

Lee, J., Cho, D., Choi, H. and Choi, J. (2007), "Concept of a Korean reference disposal system for spent fuels", *J. Nucl. Sci. Technol.*, **44**(12), 1565-1573. https://doi.org/10.1080/18811248.2007.9711407.

Lee, J., Kim, I., Ju, H.J., Choi, H. and Cho, D., (2020), "Proposal of an improved concept design for the deep geological disposal system of spent nuclear fuel in Korea", *J. Nucl. Fuel Cycle Waste Technol.*, **18**, 1-19. https://doi.org/10.7733/jnfcwt.2020.18.S.1.

Lee, G.J., Yoon, S. and Kim, B.J. (2023), "Prediction model for saturated hydraulic conductivity of bentonite buffer materials for an engineered-barrier system in a high-level radioactive waste repository", *J. Nucl. Fuel Cycle Waste Technol.*, **21**(2), 225-234. https://doi.org/10.7733/jnfcwt.2023.017.

Lee, M., Hong, C.H., Kim, J.W., Kim, J. and Kim, J.S. (2024), "Early and post-stage piping erosion in bentonite buffer materials exposed to groundwater inflow", *Geomech. Energ. Environ.*, **40**, 100611. https://doi.org/10.1016/j.gete.2024.100611.

Li, K.P., Chen, Y.G., Ye, W.M. and Wang, Q. (2023), "Self-sealing behavior of bentonite-based materials in high-level radioactive waste disposal: A systematic review", *Appl. Clay Sci.*, **235**, 106873. https://doi.org/10.1016/j.clay.2023.106873.

Lim, H.H., Cheon, E., Lee, D.H., Jeon, J.S. and Lee, S.R. (2020), "Classification of granite soils and prediction of soil water content using hyperspectral visible and near-infrared imaging", *Sensors*, **20**(6), 1611. https://doi.org/10.3390/s20061611.

Meng, Y., Wang, Q., Su, W., Ye, W. and Chen, Y. (2023), "Experimental evidence on the cracking and sealing mechanisms of compacted bentonite by using microfocus X-ray computed tomography", *Eng. Geol.*, **322**, 107153. https://doi.org/10.1016/j.enggeo.2023.107153.

Min, D.H. and Yoon, H.K. (2024), "Prediction of dynamic soil properties coupled with machine learning algorithms", *Geomech. Eng.*, **37**(3), 253-262. https://doi.org/10.12989/gae.2024.37.3.253.

Park, S., Yoon, S., Kwon, S., Lee, M.S. and Kim, G.Y. (2021), "Temperature effect on the thermal and hydraulic conductivity of Korean bentonite buffer material", *Prog. Nucl. Energ.*, **137**, 103759. https://doi.org/10.1016/j.pnucene.2021.103759.

Persson, M. (2005), "Estimating surface soil moisture from soil color using image analysis", *Vadose Zone J.*, **4**(4), 1119-1122. https://doi.org/10.2136/vzj2005.0023.

Peron, H., Laloui, L., Hueckel, T. and Hu, L.B. (2009a), "Desiccation cracking of soils", *Eur. J. Environ. Civil Eng.*, **13**(7-8), 869-888.

Peron, H., Hueckel, T., Laloui, L. and Hu, L. (2009b), "Fundamentals of desiccation cracking of fine-grained soils: experimental characterisation and mechanisms identification", *Can. Geotech. J.*, **46**(10), 1177-1201. https://doi.org/10.1139/T09-054.

Posiva (2021), Buffer, Backfill and Closure Evolution. Posiva Working Report 2021-08. Eurajoki, Finland.

Pusch, R. (2006), "Mechanical properties of clays and clay minerals", *Develop. Clay Sci.*, **1**, 247-260. https://doi.org/10.1016/S1572-4352(05)01006-8.

Schneider, C.A., Rasband, W.S. and Eliceiri, K.W. (2012), "NIH Image to ImageJ: 25 years of image analysis", *Nature Method.*, **9**(7), 671-675.

Sellin, P. and Leupin, O.X. (2013), "The use of clay as an engineered barrier in radioactive-waste management a review", *Clays Clay Min.*, **61**, 477-498. https://doi.org/10.1346/CCMN.2013.0610601.

Shwan, B.J. (2023), "Microstructural interpretation of effective stress equations for unsaturated sands", *Int. J. Geo-Eng.*, **14**(1), 4. https://doi.org/10.1186/s40703-022-00181-8.

SKB (2022), Post-Closure Safety for the Final Repository for Spent Nuclear Fuel at Forsmark – Buffer, Backfill and Closure Process Report, PSAR Version. Technical Report TR-21-03. Solna, Sweden.

Yoon, S, Kim, M.J., Park, S. and Kim, G.Y. (2021), "Thermal conductivity prediction model for compacted bentonites considering temperature variations", *Nucl. Eng. Technol.*, **53**, 3359-3366. https://doi.org/10.1016/j.net.2021.05.001.

Yoon, S, Lee, D.H., Cho, W.J., Lee, C. and Cho, D.K. (2022), "Evaluation of water suction for compacted bentonite buffer under elevated temperature conditions", *J. Nuclear Fuel Cycle Waste Technol.*, **20**(2), 185-192. https://doi.org/10.7733/jnfcwt.2022.015.

Yoon, S, Jeong, H., Lee, H.L, Kim, T., Hong, C.H. and Kim, J.S. (2023), "Evaluation of uniaxial compression and point load tests for compacted bentonites", *Acta Geotech.*, **18**, 4633-4644. https://doi.org/10.1007/s11440-023-01844-1.

Yoon, S., Lee, G.J., Lee, D.H., Kim, M.S., Kim, J.T. and Kim, J.S. (2024), "Evaluation of thermal properties for the bentonil-WRK bentonite", *J. Nucl. Fuel Cycle Waste Technol.*, **22**(1), 9-16. https://doi.org/10.7733/jnfcwt.2024.008.

Villar, M.V., Iglesias, R.J., Gutiérrez-Álvarez, C. and Carbonell, B. (2018), "Hydraulic and mechanical properties of compacted bentonite after 18 years in barrier conditions", *Appl. Clay Sci.*, **160**, 49-57. https://doi.org/10.1016/j.clay.2017.12.045.

Villar, M.V., Iglesias, R.J., García-Siñeriz, J.L., Lloret, A. and Huertas, F. (2020), "Physical evolution of a bentonite buffer during 18 years of heating and hydration", *Eng. Geol.*, **264**, 105408. https://doi.org/10.1016/j.enggeo.2019.105408.

Wang, Q., Meng, Y., Su, W., Ye, W. and Chen, Y. (2021), "Cracking and sealing behavior of the compacted bentonite upon technological voids filling", *Eng. Geol.*, **292**, 106244. https://doi.org/10.1016/j.enggeo.2021.106244.